Computers and Fluids 132 (2016) 1–9

Contents lists available at ScienceDirect

Computers and Fluids

journal homepage: www.elsevier.com/locate/compfluid

Spectrally accurate Stokes eigen-modes on isosceles triangles

Lizhen Chen[a], Gérard Labrosse[a], Pierre Lallemand[a], Li-Shi Luo[a,b,*]

[a] Beijing Computational Science Research Center, Beijing 100193, China
[b] Department of Mathematics and Statistics, Old Dominion University, Norfolk, Virginia 23529, USA

ARTICLE INFO

Article history:
Received 25 May 2015
Revised 4 January 2016
Accepted 3 March 2016
Available online 18 March 2016

Keywords:
Stokes eigen-modes on isosceles triangles
Spectral methods
Weyl asymptotic formula
Linear stream function-vorticity correlation

ABSTRACT

We numerically study the Stokes eigen-modes in two dimensions on isosceles triangles with apex angle $\theta = \pi/3,\ \pi/2$, and $2\pi/3$ by using two spectral solvers, *i.e.*, a Lagrangian collocation method with a weak formulation for the primitive variables and a Legendre–Galerkin method for the stream-function. We compute the first 6,400 Stokes eigen-modes. With 72 collocation points in each spatial dimension, the eigen-values λ_n for $n \leq 400$ can be obtained with spectral accuracy and at least ten significant digits. We show the symmetry of the Stokes eigen-modes dictated by the geometry of the bounded flow domain. From the spectrally accurate data of the Stokes eigen-modes, the following features are observed. First, the n-dependence of the spectrum λ_n obeys the Weyl asymptotic formula in two dimensional space: $\lambda_n = C_1 n + C_2\sqrt{n} + o(\sqrt{n})$. Second, for an isosceles triangle with legs of unit length, the θ-dependence of the spectrum λ_n can be accurately approximated by $\lambda_n(\theta)/\lambda_n(\pi/2) \approx 1/(\sin\theta)$, as a consequence the volume-dependence of the coefficient C_1 in the Weyl asymptotic formula. And third, a linear stream function-vorticity correlation is observed in the interior of the flow domain.

1. Introduction

The accurate numerical determination of eigen-spaces is generally far more demanding than solving the associated inhomogeneous differential equations, especially for nonlinear problems. This is particularly acute for the Stokes eigen-space in closed domain, for which the objective was achieved only recently, and only for simple domains of a square in two dimensions (2D) and a cube in three dimensions (3D) [1–4]. The endeavor to study Stokes eigen-modes has a great significance for it opens an interesting window to the understanding of the Navier-Stokes physics itself [4]. In addition, the Stokes eigen-modes can be of interest for various applications, such as the behavior of living tissues subject to stresses [5].

In this work we will study the Stokes eigen-modes on isosceles triangles in 2D with apex angle $\theta = \pi/3$ (60°), $\pi/2$ (90°), and $2\pi/3$ (120°), which are equilateral, right, and obtuse isosceles triangles, respectively. In particular, we will use spectral methods to compute the Stokes eigen-modes on the isosceles triangles and validate our results with high precision by using two spectral solvers. The first spectral solver is based on a Lagrangian collocation method with a weak formulation for primitive variables, and the second one is based on a Legendre–Galerkin method for the stream-function.

The remainder of this paper is organized as follows. Section 2 describes the Stokes eigen-value problem and the spectral solvers to be used in sufficient details. Section 3 presents the main numerical results of this work, which include the first 20 Stokes eigen-values and corresponding eigen-modes for the isosceles triangles with the apex angle $\theta = \pi/3,\ \pi/2$, and $2\pi/3$. Section 4 discusses some properties of the Stokes spectrum $\{\lambda_n\}$, including its dependence on n and θ, and the stream function-vorticity correlation. Finally, Section 5 concludes the paper.

2. The Stokes equations and spectral solvers

2.1. Stokes equations

We will consider the following time-dependent Stokes equations for the primitive variables in dimensionless form:

$$\partial_t \boldsymbol{u} = \Delta \boldsymbol{u} - \nabla p, \quad \nabla \cdot \boldsymbol{u} = 0, \qquad (\boldsymbol{x}, t) \in \Omega \times (0, T], \tag{1}$$

where $\boldsymbol{u}(\boldsymbol{x}, t) := (u, v)$ is the flow velocity, $p(\boldsymbol{x}, t)$ is the pressure, and $\Delta := \nabla \cdot \nabla := \nabla^2$ is the Laplacian operator; T is a real positive number, and the flow domain Ω is an open isosceles triangle, as illustrated in Fig. 1. The origin of the plane coordinate system (x, y) is set on the centroid of the triangle, as shown in Fig. 1. Proper initial and Dirichlet boundary conditions are imposed on the velocity $\boldsymbol{u}$. The eigen-problem is defined by $\partial_t \boldsymbol{u} = -\lambda \boldsymbol{u}$, where

* Corresponding author at: Department of Mathematics and Statistics, Old Dominion University, Norfolk, Virginia 23529, USA. Tel.: +1 7576835295; fax: +1 7576833885.
E-mail addresses: lzchen@csrc.ac.cn (L. Chen), labrossenator@gmail.com (G. Labrosse), pierre.lal@free.fr (P. Lallemand), lluo@odu.edu (L.-S. Luo).

http://dx.doi.org/10.1016/j.compfluid.2016.03.004
0045-7930/

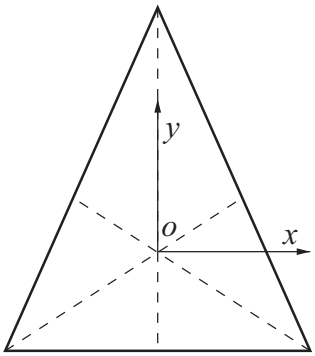

Fig. 1. Illustration of an isosceles triangle. The dashed lines are the bisectors. The origin of the plane coordinate system (x,y) sits at the centroid of the triangle.

$-\lambda$ is the algebraic temporal growth rate of $\boldsymbol{u}$, *viz.*, the Stokes eigen-value. Thus the eigen-system reads as the following,

$$-\lambda \boldsymbol{u} = \Delta \boldsymbol{u} - \nabla p, \quad \nabla \cdot \boldsymbol{u} = 0, \quad \boldsymbol{x} \in \Omega, \tag{2a}$$

$$\boldsymbol{u} = \boldsymbol{0}, \quad \boldsymbol{x} \in \partial\Omega, \tag{2b}$$

where $\partial\Omega$ denotes the boundary of flow domain Ω.

An alternative formulation of the system (2) is based on the vector-potential. This leads to a 2D bi-harmonic system for the stream function $\psi(x,y)$, which is the vector potential component normal to the flow plane. This system reads

$$\Delta^2 \psi = -\lambda \, \Delta \psi, \quad \boldsymbol{x} \in \Omega, \tag{3a}$$

$$\psi = 0 = \frac{\partial \psi}{\partial \hat{\boldsymbol{n}}}, \quad \boldsymbol{x} \in \partial\Omega, \tag{3b}$$

where $\hat{\boldsymbol{n}}$ is the unit vector out-normal with respect to the flow boundary $\partial\Omega$.

2.2. Spectral solvers

We use two spectral solvers to determine the Stokes eigen-space. Both solvers are based on a weak formulation of the problem. With the Duffy mapping [6], a triangle is mapped onto a square wherein the mathematical problem is solved [6–9]. The mapping transforms each differential operator of the problem into a combination of mixed partial derivative operators multiplied by a function of the new coordinates [10,11]. With the Duffy mapping, the basis functions are endowed with the full tensorial product property on arbitrary triangular domain in 2D and tetrahedral domain in 3D. This allows a greater flexibility in handling complex domains while retaining all the essential features of the usual spectral element method [10–12].

Fig. 2 illustrates the Gauss–Lobatto–Legendre collocation points with $N = 10$, which are mapped from a square to an isosceles triangle. The figure clearly demonstrates the accumulation of collocation points at the apex of the triangle due to the mapping. It has been observed that, for non-equilateral triangles, the numerical results are independent of the choice of apex in the mapping.

The first solver is a Lagrangian collocation method in weak form for the system (2) of the primitive variables, which can be written in the following matrix form before the mapping:

$$\begin{pmatrix} \Delta & 0 & \partial_x \\ 0 & \Delta & \partial_y \\ \partial_x & \partial_y & 0 \end{pmatrix} \begin{pmatrix} u \\ v \\ p \end{pmatrix} = -\lambda \begin{pmatrix} 1 & 0 & 0 \\ 0 & 1 & 0 \\ 0 & 0 & 0 \end{pmatrix} \begin{pmatrix} u \\ v \\ p \end{pmatrix}. \tag{4}$$

After mapping, each resulting new system is projected onto a set of basis functions, which are tensorial products of Lagrange polynomials. For the velocities (u,v), the Lagrange polynomials are based on Gauss–Lobatto–Legendre points defined on a square, whereas

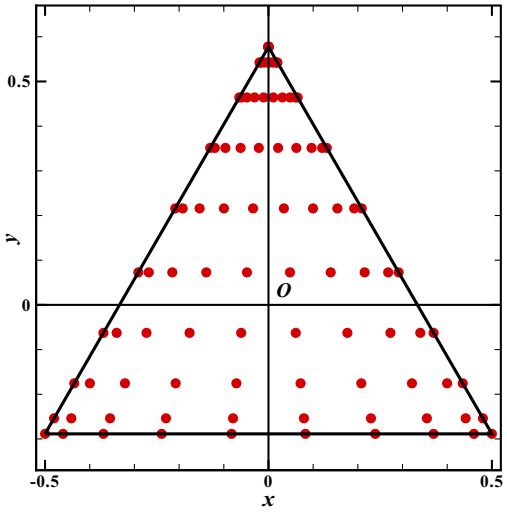

Fig. 2. The Gauss–Lobatto–Legendre collocation points in the equilateral triangle ($\theta = 60^\circ$) for $N = 10$.

for the pressure p, the collocation points are Gauss–Legendre ones. This is thus a staggered-grid system, the so-called $P_N \times P_{N-2}$ option, which is free of any spurious pressure mode.

The second solver is based on the stream-function formulation (3) discretized by a Legendre–Galerkin method. The basis functions are tensorial products of appropriate 3-term linear combination of Legendre polynomials on a square [13].

The projections are made by using quadrature in both solvers. With N points in each dimension, they lead to linear systems of sizes $3(N-2)^2$ and $(N-4)^2$ for the primitive-variable (PV) and the stream function (SF) solvers, respectively. The linear system is solved by using the LAPACK routine `dggev`, which is based on the the generalized Schur decomposition (the QZ decomposition). The computational complexity is $O(M^3) = O(N^6)$ for both matrix construction and the solution of the eigenvalue problem (by using the QZ decomposition), where M is the total number of collocation points or the dimension of the matrix. Using one core of a 32-core Intel® 2.67GHz Xeon® CPU, for the SF solver, the single-core CPU times for matrix construction are 491 s and 1293 s for $N = 72$ and 84, respectively; and the corresponding CPU times for the eigenvalue problem are 2146 s and 5622 s.

We first validate these two solvers by carrying out computations with $N = 24$, 36, and 48 for the PV solver and $N = 24$, 36, 48, 60, 72, and 84 for the SF solver. Their results agree well with each other. However, for a given N, the SF solver yields significantly more accurate results than the PV solver, as observed previously [14]. Therefore, the numerical results presented later are obtained by using the SF solver with $N = 84$, unless otherwise stated. The accurate significant digits of the numerical results are determined by comparing the results obtained with $N = 72$ and that with $N = 84$.

A general comment about the accuracy of spectral methods to compute the eigen-value problem is in order here. For the elliptic eigen-value problems of order 2 m in d dimensional space, the number of the eigen-values which can be reliably computed with spectral methods is bounded by $N^d(2/\pi)^{dm}$ under the most favorable situation, *i.e.*, eigen-functions are sufficiently smooth and round-off errors are not considered [15]. In this work, $N = 72$, $d = 2$, and $m = 2$ with respect to the stream-function ψ, thus $N^d(2/\pi)^{dm} \approx 850$. The first few eigen-values, λ_n for $n < 350$, are thus accurate for at least twelve digits. As shown later, our results indicate that we have indeed achieved the expected spectral accuracy with our methods.

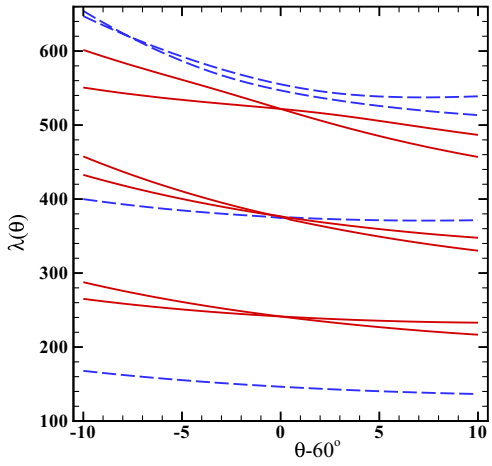

Fig. 3. The θ-dependence of the first ten eigen-values $\lambda_n(\theta)$ for an isosceles triangle with apex angle θ. The solid and dashed lines correspond to doublets and singlets of Stokes eigen-modes for the equilateral triangle ($\theta = 60^\circ$), respectively.

3. The Stokes eigen-modes

In this section we will present the numerical results of Stokes modes. The normalization used in this work, unless otherwise stated, is that the length of the legs of an isosceles triangle is set to be unity, thus the area of an isosceles triangle with apex angle θ is $A(\theta) = (\sin\theta)/2$.

3.1. Symmetries of the Stokes eigen-modes

Before presenting the numerical results for the Stokes eigen-values, we shall briefly discuss the symmetry properties of the eigen-modes. Obviously, the symmetry of the eigen-modes is dictated by that of the Stokes eigen-system (3) with the associated boundary conditions. In particular, the symmetry of the eigen-modes must reflect the geometrical symmetry of the flow domain.

The eigen-systems (2) and (3) on an isosceles triangle are invariant under a number of symmetry operations corresponding to permutations of vertices, *i.e.*, crystallographic point group. For the equilateral triangle, the symmetries include three-fold rotation about its centroid in addition to the reflections, which form the dihedral group $\mathfrak{D}_3$ of order six. For the non-equilateral isosceles triangles, there is only the symmetry of the reflection about the vertical height, which form the group $\mathfrak{C}_2$ of order two. The group $\mathfrak{D}_3$ can be decomposed into subgroups of rotations and reflections. Accordingly, the set of the Stokes modes is invariant under these symmetry operations and can be classified into subsets similar to what has been done in crystallography [16].

For the equilateral triangle ($\theta = \pi/3$), the eigen-value λ_n is either non-degenerate or degenerate with a two-fold degeneracy, corresponding to the modes classified as singlet or doublet, respectively. Non-equilateral isosceles triangles do not possess the three-fold rotational symmetry. Consequently the eigen-systems (2) and (3) only accommodate singlets that are either symmetric or anti-symmetric with respect to the height, *i.e.*, the symmetry of the group $\mathfrak{C}_2$. Therefore, for the equilateral triangle, there exist singlet modes which respect the three-fold rotational symmetry and doublet modes which are either symmetric or anti-symmetric about the height. For the non-equilateral isosceles triangles, there only exist symmetric and anti-symmetric singlet modes.

To illustrate the θ-dependence of the eigen-value λ_n related to its symmetry property, we show in Fig. 3 the first ten Stokes eigen-values $\lambda_n(\theta)$ of an isosceles triangle with its apex angle θ varying in the range of $60^\circ \pm 10^\circ$. These ten eigen-modes include four singlets and three doublets when $\theta = 60^\circ$. These calculations are done by using a validated lattice-Boltzmann solver for the Stokes flows [2,4].

The figure clearly shows that the doublets consisting of a symmetric and an anti-symmetric mode split to two singlets as soon as the apex angle θ deviates from 60°. When θ deviates from 60°, all singlet modes lose the three-fold rotational symmetry but maintain the reflective symmetry about the vertical height, thus become symmetric modes, while each doublet mode splits into two distinctive ones, one symmetric and another anti-symmetric.

3.2. Numerical results of the Stokes eigen-modes

We first show the contour plots of the stream function ψ associated with the first five Stokes eigen-modes for the equilateral triangle ($\theta = 60^\circ$) in Fig. 4, and the same for the right isosceles triangle ($\theta = 90^\circ$) and the obtuse isosceles triangle ($\theta = 120^\circ$) in Fig. 5.

Clearly, all the eigen-modes obey the reflective symmetry with respect to the vertical height, as shown in all the stream-function contours shown in Figs. 4 and 5. The eigen-modes are either symmetric or anti-symmetric with respect to the height, and they are denoted by $|+\rangle$ and $|-\rangle$, respectively. For the equilateral triangle ($\theta = 60^\circ$), the singlets have the three-fold rotational symmetry, as shown in the left column of Fig. 4. The three-fold rotational symmetry is responsible for the existence of the singlet and doublet modes. This symmetry is due to the cyclic-permutation symmetry of vertices of a triangle, similar to the cyclic-permutation symmetry on a square in 2D or a cube in 3D [4]. It can be shown in this cyclic-permutation framework that the singlets and doublets are intimately connected with each other, *i.e.*, they are generated together [4]. This means that the number of singlets and that of doublets are equal. In the continuous space there are an infinite number of modes. One should then observe that a singlet and a doublet emerge together in a pair, of which the eigen-values may or may not be consecutive. In the discrete case, the finite number of eigen-modes we have access to is $(N-4)^2$, where N is the number of collocation points in one dimension.

We note that the Moffat corner eddies [17] are present in all the eigen-modes, even if they are not visible in the contour plots of the stream function in Figs. 4 and 5. For example, for the obtuse triangle ($\theta = 120^\circ$), the corner eddies are not seen near the apex in Fig. 5, but they do exist.

The numerical results for the first twenty Stokes eigen-values of λ_n are tabulated in Table 1. The values of λ_n given in Table 1 are accurate for at least eleven significant digits. The accuracy is estimated by comparing the results obtained with $N = 72$ and 84. For each given apex angle θ, the Stokes eigen-values are organized according to the symmetry of the corresponding Stokes modes.

4. Properties of the triangular Stokes eigen-modes

The Stokes eigen-modes have been shown to possess the following two salient properties. First, its spectrum λ_n obeys the Weyl asymptotic formula [18–21]. It is known that the spectrum λ_n of the elliptic operator of mth order, Δ^m, on a d-dimensional manifold $\Omega \in \mathbb{R}^n$ with boundary $\partial\Omega$ obeys the Weyl asymptotic formula (cf. [21]):

$$\lambda_n = 4\pi \left[\frac{\Gamma(1+d/2)}{(d-1)\|\Omega\|} \right]^{2m/d} n^{2m/d} + \chi \kappa_d n^{(2m-1)/d} + o(n^{(2m-1)/d}), \tag{5}$$

where $d \geq 2$, Γ denotes the Gamma function, $\|\cdot\|$ denotes the Lebesgue measure (or the volume) of a set, κ_d depends on d and $\|\partial\Omega\|$, and $-1 \leq \chi \leq +1$ depends on the boundary conditions

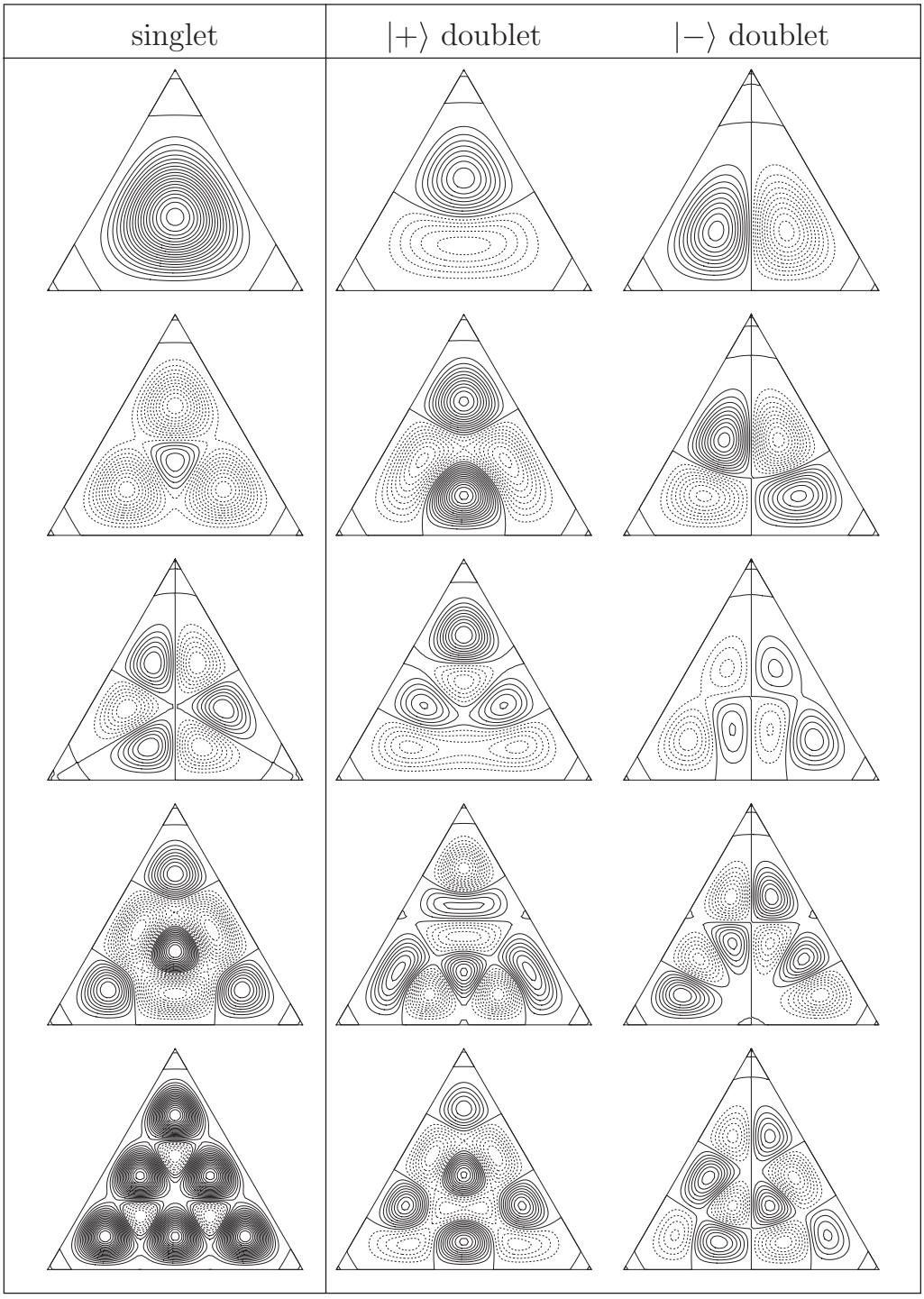

Fig. 4. The contours of the stream function ψ for first five Stokes eigen-modes in each symmetry family of an equilateral triangle. The solid and dashed lines indicate positive and negative values of ψ, respectively.

(Neumann or Dirichlet). Particular to this study, $d = 2$ and $m = 1$ with respect to the primitive variables, the coefficient of the leading order term is definitive [22–25]. A formula for $d = 2$ and $m = 1$ is given in the monograph of Courant and Hilbert [18]. And second, in the core of the eigen-modes in both 2D and 3D space, the stream function $\boldsymbol{\psi}$ and the vorticity $\boldsymbol{\omega}$ are linearly correlated to each other [1]:

$$\frac{(\boldsymbol{\omega} - \boldsymbol{\omega}_0)}{\lambda} = \gamma \boldsymbol{\psi}, \tag{6}$$

where $\boldsymbol{\omega}_0$ is a constant vorticity offset, possibly zero, and γ is a positive constant bounded by 1. The correlation (6) becomes exact with $\gamma = 1$ when the flow is fully periodic, *i.e.*, periodic in all the space directions. Thus, this correlation can be used as a measure of the periodic characteristic for the Stokes eigen-modes in the interior of a flow domain Ω bounded by non-periodic boundary conditions.

In what follows we will investigate the Stokes eigen-modes to see if they obey both relationships (5) and (6), and to what extent.

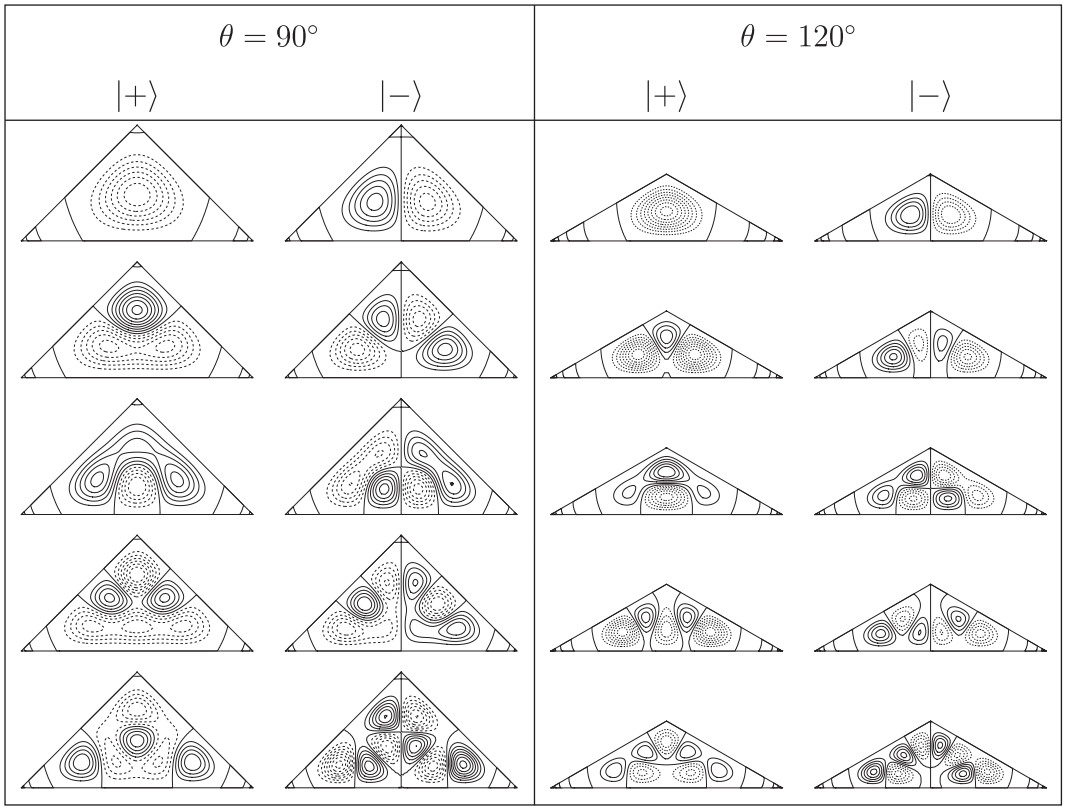

Fig. 5. The contours of the stream function ψ for the first five Stokes eigen-modes in each symmetry family of the isosceles triangle with $\theta = 90^\circ$ and 120°. The values represented by the dashed and solid lines are respectively negative and positive.

Table 1
The first 20 eigen-values for each symmetry family of the triangular Stokes eigen-modes, computed with $N = 84$, listed with significant places estimated from the results computed with $N = 72$.

$\theta = 60^\circ$		$\theta = 90^\circ$		$\theta = 120^\circ$	
Doublet	Singlet	$\|+\rangle$	$\|-\rangle$	$\|+\rangle$	$\|-\rangle$
241.25704766644	146.41290510934	139.57412735002	205.55479327727	212.09016766345	278.8491953632
376.2889061319	374.4223156617	247.86353978828	337.70781425411	350.2520641513	428.3413974258
521.4130857962	546.4713794567	304.58865427625	415.27027186594	437.4237298435	562.6399229516
706.2874049870	554.9855425810	404.38637279961	509.6946658122	514.7051132068	610.6006112033
760.0725853370	707.7866772738	458.27549996923	585.9687054998	649.891515593	761.406013098
907.117621846	924.5928500885	556.87419675850	705.9458089401	713.489414858	827.517350736
1004.697876348	939.4055583177	600.13523668017	726.6810138625	795.676687991	958.824310564
1143.070171871	1146.4312782970	648.9953007758	797.3220099562	876.28819894	1007.309357540
1192.769262814	1283.1970131587	745.5289759024	913.935439189	950.22284363	1082.524598015
1398.201651846	1286.3885527477	834.0986091571	978.97003340629	1059.96899642	1203.600398732
1488.485364339	1411.491255036	880.7513699219	1047.559550482	1127.05247942	1277.876796156
1600.203822871	1429.8602201220	892.8753171180	1083.067429084	1215.188498065	1373.434277614
1685.785186415	1690.353400796	976.0575876511	1163.90421307	1249.846310970	1460.724123867
1733.190888344	1816.472786969	1107.036870560	1273.078531316	1337.70021345	1503.222645213
1950.727132674	1824.0178866374	1119.760839765	1323.23787176	1421.19382799	1581.863699604
1994.618435299	2005.231095544	1153.405240803	1341.7275849385	1527.12379747	1698.411288530
2080.164291765	2025.891988185	1246.2838439777	1453.83256393448	1576.36050481	1755.920413764
2187.584786015	2335.602382840	1304.557298127	1535.200754437	1637.55766511	1826.83063467
2334.108911264	2337.208699629	1382.3869201728	1606.465503651	1742.40049342	1923.02321879
2380.07952647	2339.56883445	1427.9592380995	1613.155580298	1807.09829079	2051.72041130

4.1. The n*-dependence of the spectrum* λ_n

We first study the n-dependence of the spectrum $\{\lambda_n\}$. The insert of Fig. 6 shows the λ_n *versus* n in log-log scales. At large n, λ_n increases with n rapidly, indicating that the discretization is no longer accurate enough to capture the Stokes eigen-modes of high wave-numbers with a given number of collocation points N^2. With $N = 72$, we can compute λ_n with an accuracy of at least ten significant digits for $n \leq 400$. The main plot of Fig. 6 shows the spectrum $\{\lambda_n\}$ for $n \leq 202$, which is the initial part of the inserted plot, *i.e.*, the slowly varying initial part of $\{\lambda_n\}$.

In Fig. 6, the labels 1 and 2 denote the singlet and doublet of the equilateral triangle ($\theta = 60^\circ$), 3 and 4 for the $|+\rangle$ and $|-\rangle$ states for the right isosceles triangle ($\theta = 90^\circ$), and 5 and 6 for the $|+\rangle$ and $|-\rangle$ states for the obtuse isosceles triangle ($\theta = 120^\circ$), respectively. We observe from the data given in Table 1 that

$$\lambda_n^{[6]} > \lambda_n^{[5]} > \lambda_n^{[4]} > \lambda_n^{[3]},$$

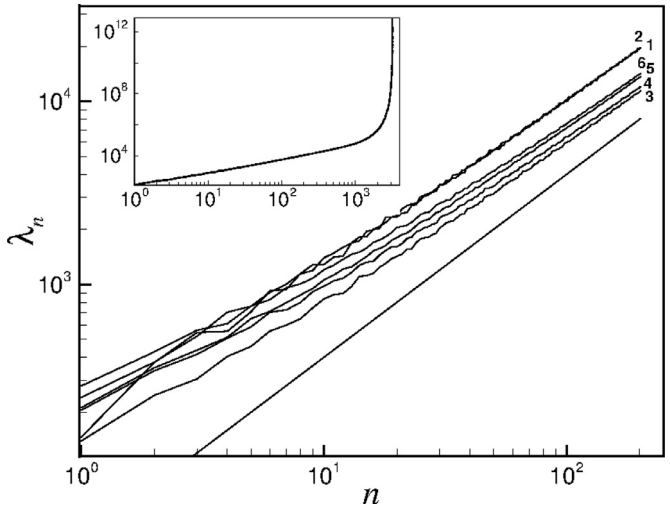

Fig. 6. Log-log plot of the Stokes spectrum, $\{\lambda_n\}$ for $n \le 202$. In the main plot, the labels 1 and 2 refer, respectively, to the singlet and doublet eigen-values of the equilateral triangle ($\theta = 60^\circ$), 3 and 4 to the $|+\rangle$ and $|-\rangle$ states in the right isosceles triangle ($\theta = 90^\circ$), and 5 and 6 to the $|+\rangle$ and $|-\rangle$ states in the obtuse isosceles triangle ($\theta = 120^\circ$). The straight line corresponds to the law of $\lambda_n = n$. The inserted plot shows a complete spectrum.

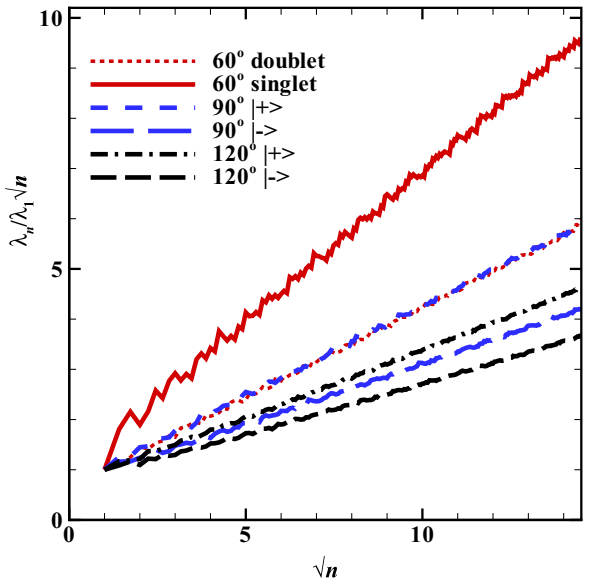

Fig. 7. $\lambda_n/(\sqrt{n}\lambda_1)$ as functions of $\sqrt{n}$ for $n \le 202$. The spectra $\{\lambda_n | n \le 202\}$ are those shown in Fig. 6.

where the superscript in square brackets [ ] indicates the mode defined previously. However, there is no such relationship between $\lambda_n^{[1]}$ and $\lambda_n^{[2]}$. Denote λ_n^+ and λ_n^- as the eigen-values corresponding to symmetric ($|+\rangle$) and anti-symmetric ($|-\rangle$) state, respectively. We observe that $\lambda_n^- > \lambda_n^+$ for both $\theta = \pi/2$ and $2\pi/3$. The reason is that in the vicinity of the apex vertex, the stream function ψ of a $|-\rangle$ state has greater curvature than that of the $|+\rangle$ state with the same n, thus the local stress of the $|-\rangle_n$ state near the apex vertex is greater than that of the $|+\rangle_n$ state.

To check if the spectrum $\{\lambda_n\}$ obeys the Weyl asymptotic formula (5), we assume that

$$\frac{\lambda_n}{\lambda_1} \approx C_1 n + C_2\sqrt{n}, \tag{7}$$

or equivalently,

$$\frac{1}{\sqrt{n}}\frac{\lambda_n}{\lambda_1} \approx C_1\sqrt{n} + C_2, \tag{8}$$

where the constant coefficients C_1 and C_2 are determined numerically for $n \le 202$. That is, the same data in Fig. 6 is used to compute both C_1 and C_2 by using the least-square fitting. Fig. 7 shows $\lambda_n/(\sqrt{n}\lambda_1)$ as functions of $\sqrt{n}$. Clearly, $\{\lambda_n/(\sqrt{n}\lambda_1) | n \le 202\}$ are well approximated by the linear function of $\sqrt{n}$ given by Eq. (8).

To quantify if the spectra $\{\lambda_n\}$ indeed satisfies the Weyl asymptotic formula (8), we cut a band of width w along the boundary off the triangular flow domain Ω; the remaining mutilated domain, which is interior of and similar to the full flow domain Ω, is denoted as Ω_w. We use the least-square method to compute the coefficients C_1 and C_2 and their standard deviations, ΔC_1 and ΔC_2, respectively, and the standard deviation of the fitting, $\sigma_{\rm rms}$; the results are given in Table 2. The data in Table 2 indicate that the standard deviations ΔC_1 for the leading order coefficient C_1 are rather small; the largest one is about 0.3% for the family of singlet modes with $\theta = 60^\circ$. In general, the standard deviations ΔC_2 for the second order coefficient C_2 are about one order of magnitude larger than the corresponding ΔC_1 for the same symmetry family of eigen-modes. It is interesting to note that $C_2 > 0$ indicates that the eigen-problem in the mutilated domain Ω_w satisfies the Neumann boundary condition instead of the original Dirichlet boundary condition given by (2), which is somewhat obvious because the boundary of the mutilated domain Ω_w is *not* a stream line anymore, thus the original Dirichlet boundary condition on $\partial\Omega$ given by (2) cannot be satisfied at the boundary of the mutilated domain $\partial\Omega_w$. Since the stream lines go through the boundary $\partial\Omega_w$, the Neumann boundary condition should be considered instead. Our results conclusively verify that the spectra indeed satisfy the Weyl asymptotic formula (5). However, the coefficients C_1 and C_2 are not constant — they depend on both the apex angle θ and the symmetry of the eigen-modes.

Table 2
The coefficients C_1 and C_2 in the formula (8) and their standard deviations, ΔC_1 and ΔC_2, respectively, and the standard deviation of the formula (8), $\sigma_{\rm rms}$, obtained by the least-square fitting.

Mode	$C_1 \pm \Delta C_1$	$C_2 \pm \Delta C_2$	$\sigma_{\rm rms}$
$\theta = 60^\circ$, doublet	$0.35931 \pm 6.22 \cdot 10^{-4}$	$0.63789 \pm 6.27 \cdot 10^{-3}$	$2.94 \cdot 10^{-2}$
$\theta = 60^\circ$, singlet	$0.59859 \pm 1.85 \cdot 10^{-3}$	$0.95741 \pm 1.87 \cdot 10^{-2}$	$8.79 \cdot 10^{-2}$
$\theta = 90^\circ$, $\|+\rangle$	$0.35772 \pm 6.78 \cdot 10^{-4}$	$0.68502 \pm 6.84 \cdot 10^{-3}$	$3.21 \cdot 10^{-2}$
$\theta = 90^\circ$, $\|-\rangle$	$0.23887 \pm 5.00 \cdot 10^{-4}$	$0.72265 \pm 5.04 \cdot 10^{-3}$	$2.36 \cdot 10^{-2}$
$\theta = 120^\circ$, $\|+\rangle$	$0.26988 \pm 3.94 \cdot 10^{-4}$	$0.68896 \pm 3.96 \cdot 10^{-3}$	$1.86 \cdot 10^{-2}$
$\theta = 120^\circ$, $\|-\rangle$	$0.20221 \pm 4.87 \cdot 10^{-4}$	$0.69912 \pm 4.90 \cdot 10^{-3}$	$2.30 \cdot 10^{-2}$

4.2. The θ-dependence of the spectrum λ_n

We now investigate the θ-dependence of the spectrum λ_n. It can be seen that the θ dependence of λ_n is not monotonic. In fact, we observe that

$$\lambda_n(\theta = \pi/3) > \lambda_n(\theta = \pi/2), \quad \lambda_n(\theta = 2\pi/3) > \lambda_n(\theta = \pi/2),$$

which is also evidenced in data given in Table 1 for both $\theta = 90^\circ$ and 120°. We compute the Stokes eigen-values $\{\lambda_n\}$ as functions of the apex angle $10^\circ \le \theta \le 170^\circ$. As an example, in Fig. 8 we show $\lambda_n(\theta = \pi/2)/\lambda_n(\theta)$ for the anti-symmetric modes $|-\rangle$ with $n = 202$, which is the largest n for the cases shown in Fig. 6. As shown in the figure, $\lambda_n(\theta = \pi/2)/\lambda_n(\theta)$ can be approximated by $\sin\theta$, which is twice of the area of the triangular flow domain $A(\theta)$. We note that for the equilateral triangle ($\theta = 60^\circ$), to correctly label the eigenvalue λ_n with an index n, a doublet mode has to be counted as two states corresponding two values of n, although the two eigenvalues are equal.

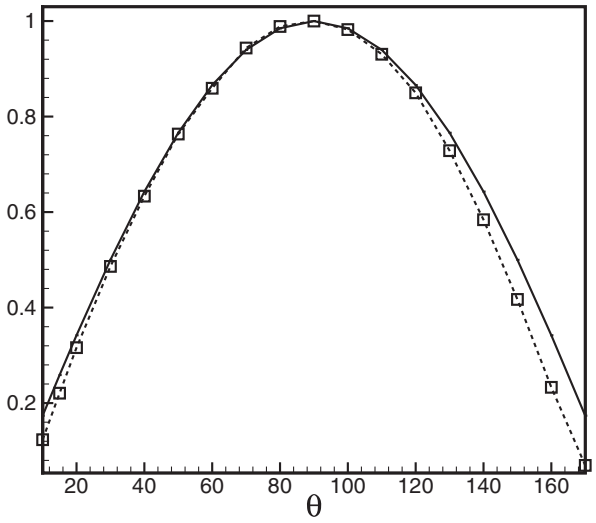

Fig. 8. Dashed line: the function $\lambda_n(\theta=\pi/2)/\lambda_n(\theta)$ with $n=202$ and for the $|-\rangle$ family of eigen-modes. Solid line: $\sin\theta$.

The figure shows that the Stokes spectrum $\{\lambda_n(\theta)\}$ within an isosceles triangle is mainly determined by the area of the triangle, $A(\theta)=(\sin\theta)/2$. More precisely, $\lambda_n(\theta)$ is proportional to $1/A(\theta)$. Therefore, the smaller the area A, the larger will be the eigen-value $\{\lambda_n\}$, hence the faster the mode to be damped out. With the legs normalized to unity, the right isosceles triangle ($\theta=90^\circ$) has the maximum area, thus the dissipation for its Stokes eigen-modes is the least and the modes decay the most slowly.

We now discuss the discrepancies between $\lambda_n(\pi/2)/\lambda_n(\theta)$ and $\sin\theta$ shown in Fig. 8. The stream function ψ has large curvatures in the vicinities near the three vertices of the triangle (cf. Figs. 4 and 5), which leads to large stresses in these regions. And, the sharper an angle, the larger the curvature, thus the larger the stress. An acute isosceles triangle with a very sharp apex angle has two base angles close to $\pi/2$, thus the stress is large only in the vicinity near the apex vertex, but relatively small in the regions near both base vertices. However, an obtuse isosceles triangle with its apex angle θ close to π has two very sharp base angles, hence the stress is large in the regions near both base vertices, but relatively small in the vicinity near the apex vertex. In other words, the obtuse triangle has two very sharp (base) angles, while the acute triangle has only one sharp (apex) angle, which means the stress in the former is roughly about twice of the latter in the vicinities of the three vertices and this is precisely seen in Fig. 8. In Fig. 8 it can be clearly seen that $\lambda_n(\pi/2)/\lambda_n(\theta) < \sin\theta$ near both limits of $\theta=0^\circ$ and $\theta=180^\circ$, while near $\theta=90^\circ$, $\lambda_n(\pi/2)/\lambda_n(\theta) \approx \sin\theta$. Also, $\lambda_n(\pi/2)/\lambda_n(\theta) > \lambda_n(\pi/2)/\lambda_n(\pi-\theta)$ for small θ. In fact, for $\varphi=10^\circ$, we can compute that

$$\frac{\lambda_n(\pi/2)}{\lambda_n(\varphi)}-\frac{1}{\sin\varphi}\approx 0.0503,$$
$$\frac{\lambda_n(\pi/2)}{\lambda_n(\pi-\varphi)}-\frac{1}{\sin(\pi-\varphi)}\approx 0.1090,$$

and $0.1090 \approx 2\times 0.0503$. We note that the $\sin\theta$ law holds for the entire spectrum $\{\lambda_n\}$, that is, it is *independent* of n. This result is obvious because of the Weyl formula (5) — the coefficient of the leading-order term is indeed proportional to $1/A(\theta)$ for the Stokes case, and the correction is proportional to $1/\sqrt{L}$, where L is the perimeter of the triangle.

4.3. Stream function-vorticity correlation

Fig. 9 shows the stream function-vorticity correlation, *i.e.*, ω/λ_n as a function of ψ. We compute ω/λ_n over the entire flow domain Ω as well as on a mutilated domain Ω_w for some chosen modes. In particular, we select six modes (cf. data in Table 1), one from each symmetry family for each apex angle: the singlet mode with $n=2$ the doublet mode with $n=1$ for $\theta=60^\circ$; $|+\rangle$ with $n=2$ and $|-\rangle$ with $n=1$ for $\theta=90^\circ$; and $|+\rangle$ with $n=2$ and $|-\rangle$ with $n=1$ for $\theta=120^\circ$. On the entire domain Ω, both the vorticity $\omega(x,y)$ and the stream function $\psi(x,y)$ are computed with *all* the collocation points, of which the number is N^2, whereas on the mutilated domain Ω_w, ω and ψ are computed with only those collocation points within Ω_w, of which the number is less than N^2, depending on the width of cut-off band w. The first and third columns in Fig. 9 show the butterfly-shaped correlation ω/λ_n as a function of ψ computed on the entire triangular flow domain Ω for the six chosen eigen-modes. These correlations are very similar to those observed in a square and a cube [3]. The butterfly shape of $\omega(\psi)/\lambda_n$ will shrink, almost, to a straight line, *i.e.*, the linear correlation of Eq. (6), when the function $\omega(\psi)/\lambda_n$ is computed on a mutilated domain Ω_w, which is obtained by cutting off a band of width w along the edges of the entire domain Ω.

We can numerically quantify the vorticity-stream function correlation $\omega(\psi)/\lambda$ on the mutilated domain Ω_w with a a band of variable width w along the boundary cut off the triangular flow domain Ω. We can compute the vorticity-stream function correlation $\omega(\psi)/\lambda$ as a function of the cut-off band width d which is parameterized by the fractional area of the mutilated triangle domain Ω_w. Assuming ω/λ is a linear function of ψ, as defined in Eq. (6), we use the least-square method to compute the slope of $\omega(\psi)/\lambda$, *i.e.*, $\gamma=\omega/\lambda\psi$ in Eq. (6), and its root-mean-square (rms) deviation $\Delta\gamma$, as functions of $A(\theta)/A_w(\theta)$, where $A(\theta)$ and $A_w(\theta)$ are the areas of Ω and Ω_w, respectively, and

$$A_w(\theta)=\frac{1}{2}\left\{1-\left[\tan\frac{\theta}{2}+\cot\frac{\theta}{2}+\frac{1}{\cos(\theta/2)}\right]w\right\}^2\sin\theta, \tag{9}$$

thus,

$$\frac{A(\theta)}{A_w(\theta)}=\left\{1-\frac{2[1+\sin(\theta/2)]w}{\sin\theta}\right\}^{-2}. \tag{10}$$

Fig. 10 shows the results of the correlation coefficient γ in the stream function-vorticity correlation (6) and its root-mean-square (rms) deviation $\Delta\gamma$ for all six modes in Fig. 9 and the symmetric singlet mode with a higher spectral wave-number, corresponding to a state of $n=33$ in Fig. 6. The following observations can be made. As the width d of the cut-off band increases, thus the boundary effect decreases, the coefficient γ increases and quickly approaches an asymptotic constant, which is mode and apex angle (θ) dependent. While the rms deviation $\Delta\gamma$ decreases exponentially as w increases and the area $A_w(\theta)$ of the mutilated domain Ω_w decreases. We notice that the mode of higher-wave-number with $n=33$ has the periodic characteristic in the interior of the bounded flow domain which is significantly larger than that of the other modes of lower wave-numbers.

Fig. 11 shows the values of ω_0 and its standard deviation, $|\Delta\omega_0|$, as functions of $A(\theta)/A_w(\theta)$. It should be noted that $\omega_0=0$ for anti-symmetric modes, and this is indeed the case seen in our calculations. We note that $|\Delta\omega_0|$ does not seem to decay as $A(\theta)/A_w(\theta)$ increases for some modes (*i.e.*, $|+\rangle$ with $\theta=90^\circ$ and $n=2$ and with $\theta=120^\circ$ and $n=2$), although the rms errors are only about 1%, while it decays exponentially for other cases (*i.e.*, $|+\rangle$ with $\theta=60^\circ$ and $n=1$ and $n=33$). The evidence shows that the ψ-ω correlation is indeed valid in the mutilated interior of a

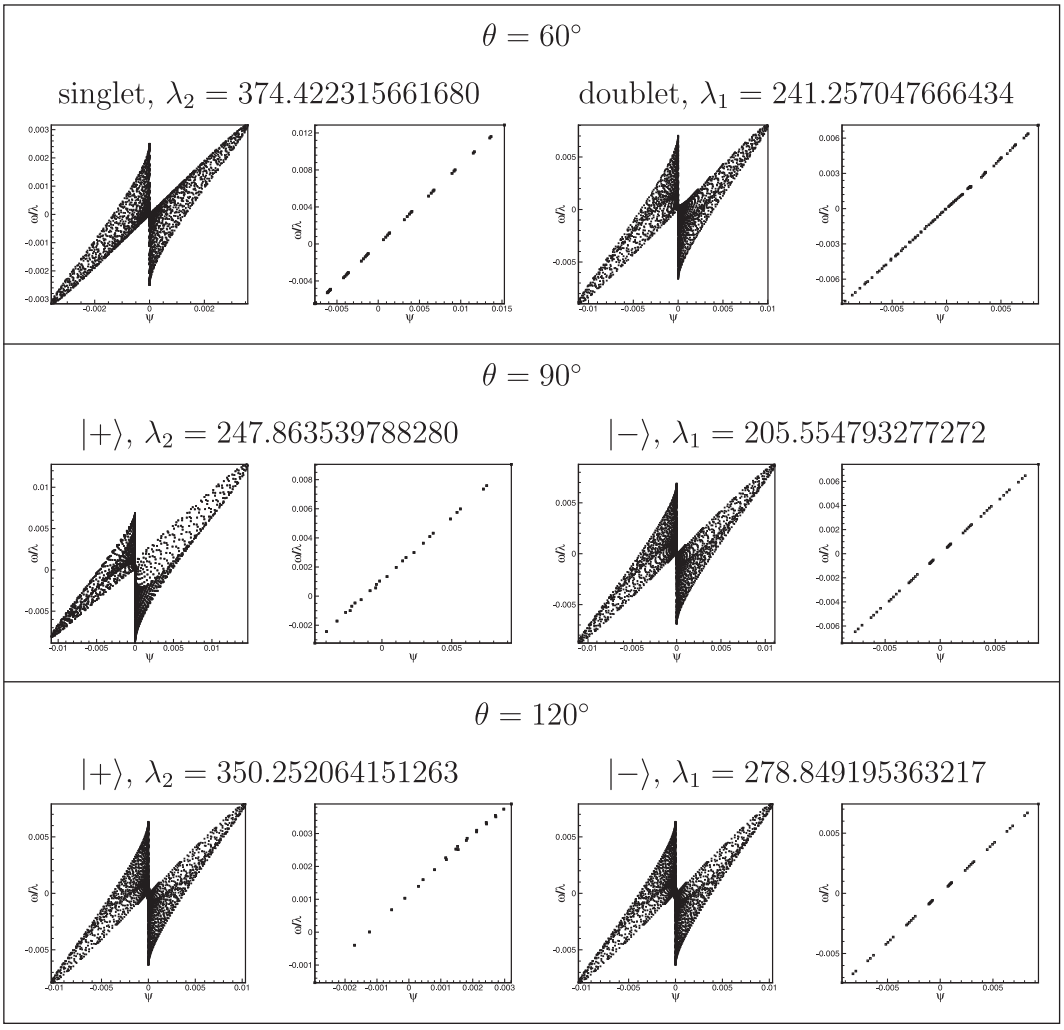

Fig. 9. The stream function-vorticity correlation, *i.e.*, ω/λ_n as a function of ψ. We select one eigen-mode per triangle and per symmetry family: the singlet mode with $n = 2$ the doublet mode with $n = 1$ for $\theta = 60^\circ$; $|+\rangle$ with $n = 2$ and $|-\rangle$ with $n = 1$ for $\theta = 90^\circ$; and $|+\rangle$ with $n = 2$ and $|-\rangle$ with $n = 1$ for $\theta = 120^\circ$. The first and third columns of plots are computed on the entire triangular flow domain Ω, the second and fourth ones are on the mutilated domain Ω_w which excludes a boundary band of width $w = 0.23$, 0.25 and 0.2 for the 60°-, 90°- and 120°-triangle, respectively.

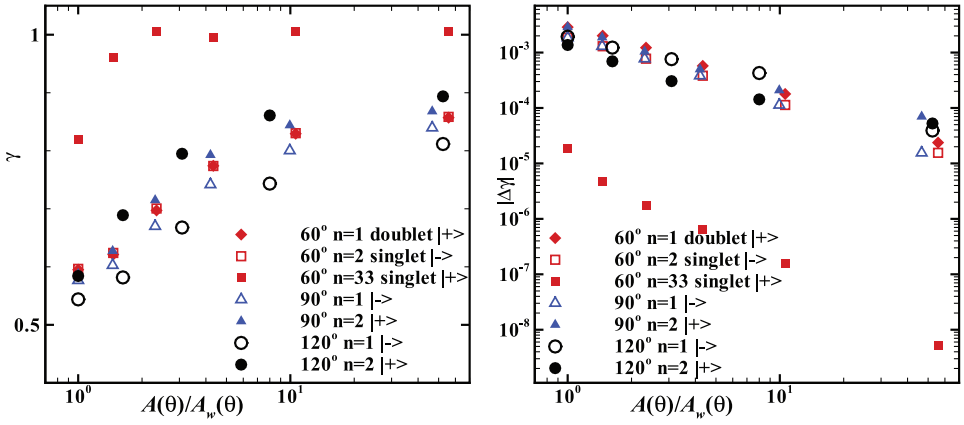

Fig. 10. Left: the correlation coefficient $\gamma = \omega/(\lambda\psi)$ as a function of $A(\theta)/A_w(\theta)$ in semi-log scale; Right: the rms deviation of γ, $\Delta\gamma$, as a function of $A(\theta)/A_w(\theta)$ in log-log scale.

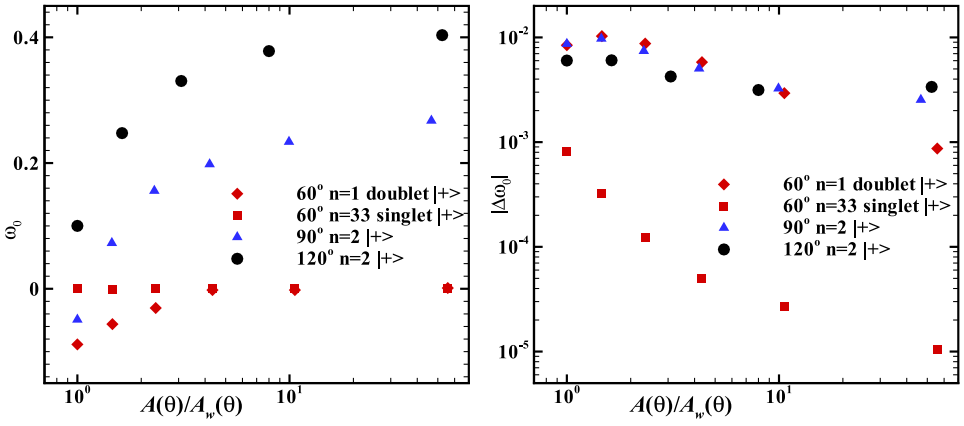

Fig. 11. Left: the off-set ω_0 as a function of $A(\theta)/A_w(\theta)$ in semi-log scale; Right: the rms deviation of ω_0, $|\Delta\omega_0|$, as a function of $A(\theta)/A_w(\theta)$ in log-log scale.

finite flow domain for the cases here, albeit the proportional factor $\gamma < 1$ for the modes of low spatial wave-numbers.

5. Conclusion

We compute the Stokes eigen-modes on isosceles triangles of apex angle $\theta = \pi/3$ (60°), $\pi/2$ (90°), and $2\pi/3$ (120°), with spectral accuracy. We use two spectral solvers to validate our results. Both solvers are based upon a weak formulation, and one is a Lagrangian collocation method for primitive variables, while the other uses the stream-function formulation. The Stokes eigen-modes are distinguished according to their symmetries, which are dictated by the flow domain. For the equilateral triangle ($\theta = \pi/3$), there are singlet and doublet modes. A singlet mode can be either symmetric or anti-symmetric about the height of the triangle, while a doublet state always consists of a symmetric mode and a anti-symmetric one. For non-equilateral isosceles triangles, there is no doublet and all modes are either symmetric or anti-symmetric.

The accurate data of eigen-modes obtained in this work allow us to observe the following important features of the Stokes modes. First, the Stokes spectrum obeys the Weyl asymptotic formula $\lambda_n = C_1 n + C_2\sqrt{n} + o(\sqrt{n})$. Second, the eigen-value is inversely proportional to the area of the triangular flow domain, *i.e.*, $\lambda_n(\theta) \propto 1/\sin\theta$, which is a consequence of the area-dependence in the coefficient C_1 of the leading order term of the Weyl asymptotic formula. And third, a linear stream function-vorticity correlation is found in the interior of the same flow domain, similar to the cases of a square in 2D and a cube in 3D. This correlation is a measure of the periodic characteristics that the confined Stokes eigen-modes enjoy in an interior of the bounded flow domain, a region whose extension increases with the spatial wave-number of the eigen-mode.

Acknowledgments

LZC would like to acknowledge the support from National Science Foundation of China (CNSF) through Grant 11301438 and Postdoctoral Science Foundation of China through Grant 2015M580038. LSL would like to thank Prof. Michel L. Lapidus and Prof. T. Yolcu for helpful discussions regarding the Weyl asymptotic formula (5) and relevant references [23–25], and Prof. Z.M. Zhang on the accuracy of numerical calculations of the eigenvalue problems [15].

References

[1] Leriche E, Labrosse G. Stokes eigenmodes in square domain and the stream function-vorticity correlation. J Comput Phys 2004;200(2):489–511.
[2] Leriche E, Lallemand P, Labrosse G. Stokes eigenmodes in cubic domain: primitive variable and lattice Boltzmann formulations. Appl Numer Math 2008;58:935–45.
[3] Leriche E, Labrosse G. Vector potential-vorticity relationship for the Stokes flows. Application to the Stokes eigenmodes in 2D/3D closed domain. Theor Comput Fluid Dyn 2007;21(1):1–13.
[4] Labrosse G, Leriche E, Lallemand P. Stokes eigenmodes in cubic domain: Their symmetry properties. Theor Comput Fluid Dyn 2014;28(3):335–56.
[5] Nelson MR, King JR, Jensen QE. Buckling of a growing tissue and the emergence of two-dimensional patterns. Math Biosci 2013;246:229–41.
[6] Duffy MG. Quadrature over a pyramid or cube of integrands with a singularity at a vertex. SIAM J Numer Anal 1982;19(6):1260–2.
[7] Owens RG. Spectral approximations on the triangle. Proc R Soc Lond A 1998;454(1971):857–72.
[8] Karniadakis GE, Sherwin SJ. Spectral/hp element methods for CFD. Oxford University Press; 1999.
[9] Braess D, Schwab C. Approximation on simplices with respect to weighted sobolev norms. J Approx Theory 2000;103(2):329–37.
[10] Chen LZ, Shen J, Xu CJ. A triangular spectral method for the stokes equations. Numer Math Theor Meth Appl 2011;4(2):158–79.
[11] Chen LZ, Shen J, Xu CJ. A unstructured nodal spectral-element method for the navier-stokes equations. Commun Comput Phys 2012;12(1):315–36.
[12] Shen J, Wang LL, Li H. A triangular spectral element method using fully tensorial rational basis functions. SIAM J Numer Anal 2009;47(3):1619–50.
[13] Shen J. Efficient spectral-Galerkin method part 1: Direct solvers of 2nd-order and 4th-order equations using Legendre polynomials. SIAM J Sci Comput 1994;15(6):1489–505.
[14] Chen W, Lin Q. Approximation of an eigenvalue problem associated with the stokes problem by the stream function-vorticity-pressure method. Appl Math 2006;51(1):73–88.
[15] Zhang ZM. How many numerical eigenvalues can we trust? J Sci Comput 2015;65(2):455–66.
[16] Kim SK. Group theoretical methods and applications to molecules and crystals. Cambridge: Cambridge University Press; 1999.
[17] Moffatt HK. Viscous and resistive eddies near a sharp corner. J Fluid Mech 1964;18:1–18.
[18] Courant R, Hilbert D. Methods of mathematical physics, vol. 1. New York: Interscience Publishers, Inc.; 1953.
[19] Métivier G. Valeurs propres de problèmes aux limites elliptiques irréguliers. Mémoires Soc Math France 1977;51-52:125–219.
[20] Métivier G. Valeurs propres des opérateurs définis sur la restriction de systèms variationnels à des sous-espases. J Math Pures Appl 1978;57:133–56.
[21] Protter MH. Can one hear the shape of a drum? Revisited. SIAM Rev 1987;29(2):185–97.
[22] Hörmander L. The analysis of linear partial differential operators, vol. IV. Berlin: Springer; 1985.
[23] Lapidus ML. Fractal drum, inverse spectral problems for elliptic operators and a partial resolution of the Weyl-Berry conjecture. Trans Am Math Soc 1991;325(2):465–529.
[24] Yolcu SY, Yolcu T. Multidimensional lower bounds for the eigenvalues of Stokes and Dirichlet Laplacian operators. J Math Phys 2012;53.
[25] Lapidus ML, Radunović G, Žubrinić D. Fractal zeta functions and complex dimensions of relative fractal drums. J Fixed Point Theory Appl 2014;15(2):321–78.